https://doi.org/10.1016/j.ijleo.2021.166366 This is the Pre-Published Version.

Influence of anisotropy factor on the memory effect: a systematic study

HONGLIN LIU[1,*], PUXIANG LAI[2,3,*] AND SHENSHENG HAN[1,4]

[1]*Key Laboratory for Quantum Optics, Shanghai Institute of Optics and Fine Mechanics, Chinese Academy of Sciences, Shanghai 201800, China*
[2]*Department of Biomedical Engineering, The Hong Kong Polytechnic University, Hong Kong SAR, China*
[3]*Hong Kong Polytechnic University Shenzhen Research Institute, Shenzhen 518000, China*
[4]*Hangzhou Institute for Advanced study, University of Chinese Academy of Sciences, Hangzhou 310024, China.*
*[5]*hlliu4@hotmail.com, and puxiang.lai@polyu.edu.hk*

Abstract: Optical angular memory effect (AME) describes a phenomenon that light remembers its incident direction even within or through a scattering medium, such as biological tissue. When the incident light beam tilts, the entire speckle pattern shifts yet maintains its morphological features within a certain range, *a.k.a*., the AME range. It is the theoretical foundation of many promising techniques, such as optical phase conjugation or wavefront shaping assisted microscopies, that have allowed us to see clearer and deeper into biological tissues. Conventional predictions in the field only take medium thickness into account, and have been proved to deviate away from practice, especially for biological tissues. Some recent explorations have improved the theory; the paraxial condition governed in most studies, however, restricts the accurate prediction to very thin layers, say, less than 300 μm even when the anisotropy factor is larger than 0.95. To explore the boundaries and promote applications of aforementioned techniques under different circumstances, a full and accurate understanding of the angular memory effect range is urgently needed. In this work, we explore the influence of anisotropy factor g on the AME range with different sample thicknesses, and an empirical relationship among the AME range, sample thickness, and g is derived and verified: as g approaches 1, the AME range yields significant enhancement; such dependence on g, however, diminishes rapidly with increased sample thickness. It confirms a rule of thumb that it is meaningful to exploit the AME only when ballistic photons or forward scattering dominate in light propagation, i.e., the penetration is within one transport mean free path.

1. Introduction

When transmitting within or through a turbid medium, photons undergo multiple scatterings and interfere with each other, resulting in randomly fluctuated intensity distributions, i.e., speckles. As the distribution of the internal refractive index inhomogeneity of the medium is out of order, currently there is no way to directly link a speckle pattern to the internal morphology of the medium, although it should be. That said, a speckle pattern is connected to the incident light beam, as represented by the famous angular memory effect (AME) that a speckle pattern remembers the direction of the incident beam [1,2]. When the incident beam is tilted within a certain range, a.k.a., the AME range, the entire speckle pattern shifts yet maintains its morphological features. Consequentially, object images can be reconstructed by speckle autocorrelation imaging [3-11] directly, or by speckle deconvolution [12], optical phase conjugation [13-17] and wavefront shaping [18-20] with a guide star, respectively. In the beginning, AME was derived as long-distance correlation in a waveguide geometry and the AME range was predicted at $\Delta\theta \approx \lambda/2\pi d$, where λ is the wavelength and d is the medium thickness [1,2]. Later, it was found that the measured AME range was significantly larger than

the theoretical prediction, especially for biological tissues with large anisotropy factors [21,22, 20]. Such a discrepancy has stimulated intensive discussion on the mechanism of memory effect [23-27]. For example, based on the macroscopic characteristics of the scattering transmission matrices of anisotropically scattering media, Judkewitz *et al.* proposed a new type of memory effect, the shift memory effect, from matrix correlations, and explained its relationship with the AME [23]; Osnabrugge *et al.* predicted a more general class of combined shift and tilt correlation in scattering media under the paraxial approximation [24]; Yilmaz *et al.* found that when light is coupled into transmission eigenchannels of scattering media, it had a larger AME range [25]. The memory effect was also found in spectral domain [26]. Recently, Liu *et al.* demonstrated that the AME was a higher order spatial shift invariance quantified by intensity correlation in space. The team derived a new formula to calculate the AME range, and modified a multiple-random-phasemask model for scattering media, which allows simulation of the wavefront propagation in the media [27]. As the paraxial condition governs in most of these studies, the prediction accuracy is limited to very thin layers, say, less than 300 μm even when the anisotropy factor is larger than 0.95. To explore the boundaries and promote applications of aforementioned techniques under different circumstances, a full and accurate understanding of the angular memory effect range is urgently needed.

In this paper, based on the aforementioned multiple-random-phasemask model, the influence of anisotropy factor g on phasemask and consequently the AME range is studied systematically. Simulation shows that the transverse correlation length of the phasemask is sensitive to g, while its contrast is only sensitive to the weight of ballistic photons in transmission. As g approaches 1, the enhancement of the AME range is significant. However, increasing the medium thickness diminishes the dependence on g quickly. Experiment results agree with the simulation quite well. It should be pointed out that the AME range plays a crucial role in determining the field of view of turbidity suppression-assisted microscopies [28-38]. This study shows that the existence of the AME depends on the weight of ballistic photons and the dominance in forward scattering. For most biological tissues, the anisotropy factor $g > 0.8$ [39,40] within the visible and near infrared regimes, and the penetration upper limit to apply the AME is one transport mean free path. Recalling that the AME range is also sensitive to the position of compensation plane, especially for a layer thinner than one transport mean free path [41]. Together it provides a gauge to maximize the field of view of different optical imaging and manipulation techniques based on the memory effect.

In the following, we first introduce the modified multiple-random-phasemask model, then simulate the time reversed focus through a scattering layer to obtain the AME range at different anisotropy factors and layer thicknesses. We also implement experiments to measure the AME ranges of tissue mimicking samples to verify the simulation. The influence of the anisotropy factor on the AME range is analyzed systematically.

2. Principle

Different from the conventional multiple-random-phasemask model that has fixed mean free path (MFP) intervals between adjacent phasemasks with each phasemask representing a single scattering event, the modified multiple-random-phasemask model has flexible intervals as shown in Fig.1. Each phasemask is constraint by the spatial power spectrum density (sPSD) consisting of ballistic and multiple scattered light components. Because of the ballistic components. the phasemasks in the modified model have lower contrast than those in the conventional ones. Here, scattering coefficient $\mu_s = 10\ mm^{-1}$ (for typical biological tissues) and anisotropy factor $g = 0.98$ are used. To have a better understanding of the modified model, let us take a close look at the individual phasemasks at different thicknesses. According to Beer's law, the intensity of ballistic light exponentially decays with the penetration thickness. As the weight of ballistic light decreases, the contrast of phasemask increases, so does the width

of the histograms. In contrast, the phasemask of singly scattered light has the highest contrast with a uniform phase distribution within $[-\pi\ \pi]$. In the meantime, the transverse coherence length, *i.e.,* the mean grain size of the phasemask, decreases with thickness.

From Ref. 27, the memory effect is a spatial shift invariance in terms of intensity correlation, and the AME range

$$\theta = \frac{\lambda}{2\pi d} \cdot \frac{\kappa}{\sqrt{2}(n-1)\sigma}, \tag{1}$$

where κ is the transverse coherence length and σ is the height deviation of a ground glass diffuser, a typical physical reality of phasemask. Within the memory effect range, changes to the input only results in a corresponding alteration to the output. The invariance range of the diffuser, however, is usually orders of magnitude smaller compared to that of a conventional shift invariance system, such as a lens system. Although we know that the sPSD of a random phasemask equals to that of a volumetric scattering medium

$$\frac{\lambda\kappa}{2\sqrt{\pi}(n-1)\sigma} \exp\left\{-\frac{\kappa^2 sin^2\theta}{[2(n-1)]^2\sigma^2}\right\} = \sum_n W_{d,n} P_n(\theta), \tag{2}$$

where $W_{d,n}$ and $P_n(\theta)$ represent respectively the weight and phase function of different components through a scattering layer of thickness d. It is difficult to derive an expression for the modification factor $\frac{\kappa}{\sqrt{2}(n-1)\sigma}$ in Eq.(1).

With the aid of the modified multiple-random-phasemask model, we can evaluate the AME range at arbitrary anisotropy factors: first, we created a point source in front of the scattering medium and recorded the wavefront of diffused light through the medium; then, we phase conjugated the wavefront to generate a focus at the original position of the point source; lastly, we loaded a phase ramp, *i.e.*, a phase grating, together with the conjugated wavefront to scan the focus along a coordinate axis and applied a curve fitting for the focal intensities at different scanning angles, whose half width at $1/e$ was selected to be the AME range. In these simulations, the interval between adjacent masks was always the MFP, and we used thicknesses of 0.5, 1, and 1.5 mm to observe how the AME range changes with the anisotropic factor g.

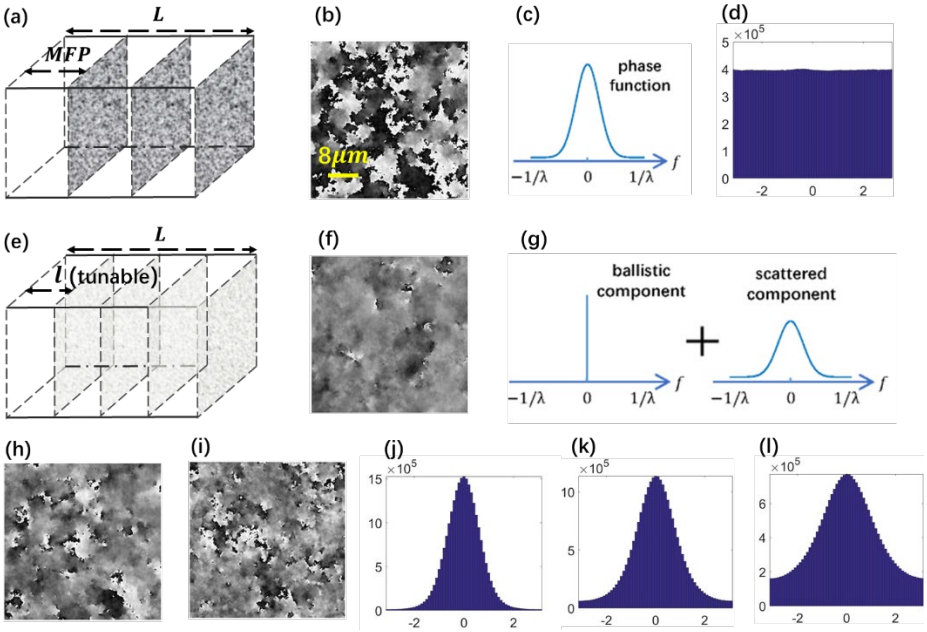

Fig. 1 Schematic illustration of the modified multiple-random-phasemask model in comparison with the conventional one. (a) In the conventional model, the interval between adjacent phasemasks is the MFP of the medium. The medium thickness $d = N * MFP$, where N is the

number of random phasemasks. The first flat screen is usually omitted. The amplitude of the Fourier Transform of a conventional phasemask (b) is determined by the phase function P(θ) (c). (d) The histogram of the conventional phasemask with a uniform distribution within $[-\pi\ \pi]$. (e) In the modified phasemask model, the interval l is tunable and the Fourier Transform of a phasemask consists a zero-frequency ballistic component and high-frequency scattering components (g). (f, h, i) Examples of modified phasemasks at different intervals $d =$ 0.5, 1, and 3 MFP, respectively, with their histograms shown in (j, k ,l).

We also made several tissue mimicking scattering samples and measured their AME ranges. The tissue mimicking scattering samples were made of silica microspheres dispersed in gelled 10% gelatin solutions. The refractive indexes of the microsphere and the background gel were 1.45 and 1.33, respectively. Two kinds of microspheres of 1 and 2.5 μm diameters were used. According to Mie Theory, the corresponding g factors are 0.95 and 0.98, respectively. The concentrations of the microspheres were controlled to be $1.35 \times 10^{-2}\ \mu m^{-3}$ and $6 \times 10^{-4}\ \mu m^{-3}$ for the 1 μm and 2.5 μm microspheres, respectively, to obtain a MFP of 0.1 mm. Fog each g, we measured two samples with 0.5 and 1 mm thicknesses, respectively. In experiment, a 532 nm laser (Readylasers, MSL-FN-532) was split into two beams, i.e., a sample beam and a reference beam (see Fig.2). In the recording step, the sample beam was coupled into a single mode fiber (Thorlabs, P1-460Y-FC-1) to create a point-like source, after which light transmitted through the scattering medium and interfered with the expanded reference beam. The fiber had a 3.5 μm diameter (the mode field diameter of the fiber), and it was placed 100 mm before the sample. The output plane of the sample was imaged onto the surface of the SLM (Holoeye, LETO) by a commercial lens L1 (Nikon, Micro-Nikkor 105mm f/2.8) with a magnification of 3x. The expanded reference beam had a diameter of 33 mm@$1/e^2$. The interference pattern on the SLM was captured by CCD1 (PCO, PCO.edge 4.2) through another commercial lens L2 (Nikon, Micro-Nikkor 105mm f/2.8). A 4-step phase shifting interferometry method [42] was implemented to extract the diffused wavefront of the sample beam. In the playback step, the end of the fiber was removed and CCD2 (Stingray, F-504B/C) was inserted into the sample beam path. The extracted wavefront was loaded on the SLM. When the reference beam was illuminated on the SLM, conjugated wavefront was generated, which traced back to the original position of the reference point and was recorded by CCD2. A phase ramp was superposed on the SLM to scan the time reversed point.

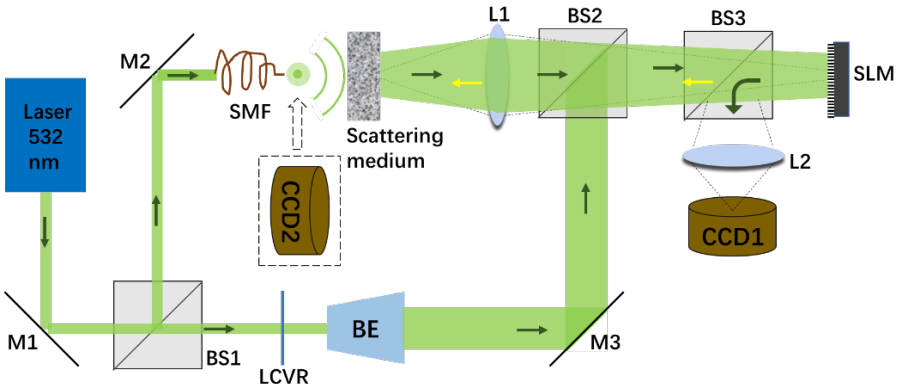

Fig. 2 Experimental setup for measuring the AME range based on time reversed focus. BS: beam splitter; L: lens; LCVR: liquid crystal variable retarder; BE: beam expander; SMF: single-mode fiber; CCD: charge coupled device; SLM: spatial light modulator; DOPC: digital optical phase conjugation.

3. Simulation and experimental results

Before simulating time reversed focus with the random multiple phasemask model, we first examined the statistical distribution change of the phasemasks with anisotropic factor g at different intervals of $d = 0.1$ and $0.5\ mm$, respectively. As shown in Figs. 3&4, the grain size decayed fast with decreased g, while the contrast keeps relatively constant for fixed thickness except for $g = 0.60\ and\ 0.40$. For simplicity, the sPSD of a scattering layer corresponding to the phasemask was obtained from Monte Carlo simulation instead of Eq.(2).

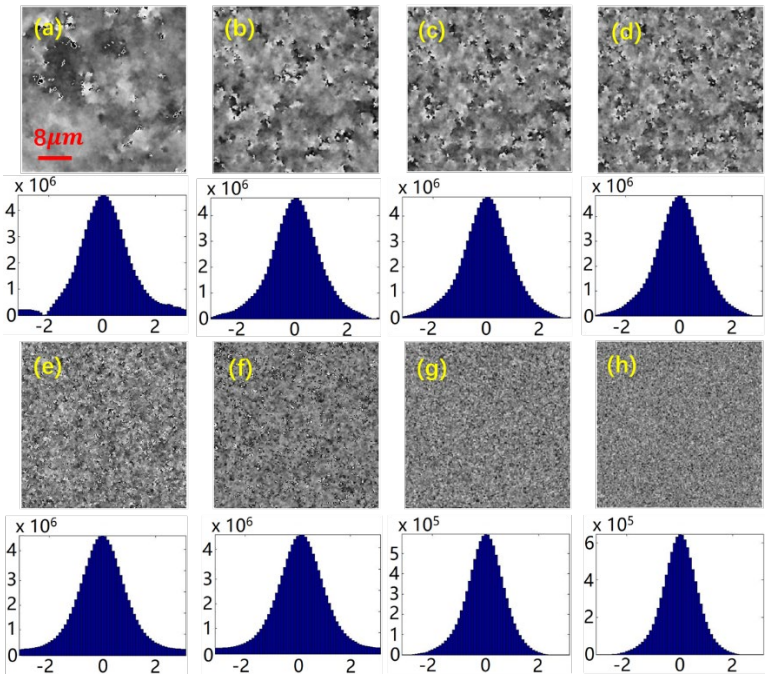

Fig. 3 Examples of phase distributions and the corresponding histograms at different anisotropic factors when $d = 0.1\ mm$. (a-h) $g = 0.98, 0.96, 0.94, 0.92, 0.90, 0.80, 0.60, and\ 0.40$, respectively.

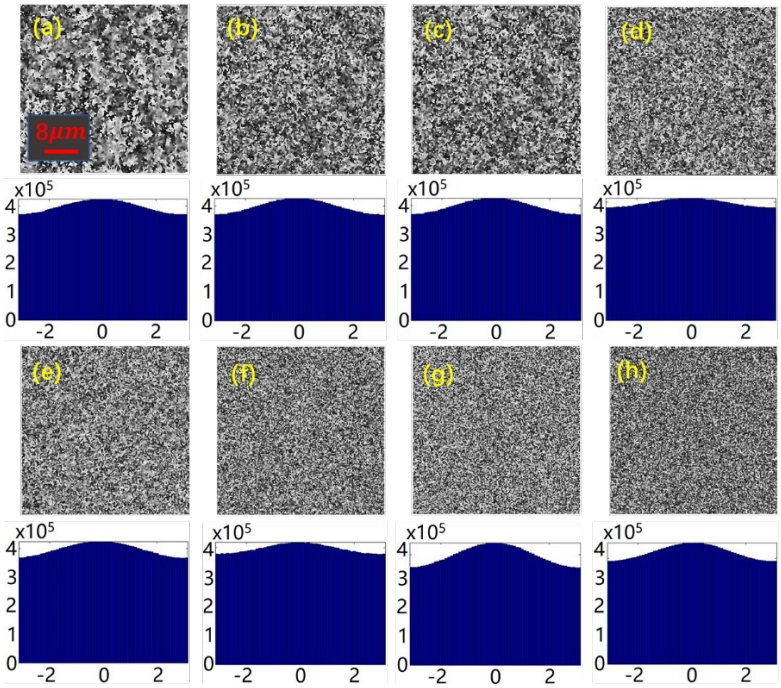

Fig. 4 Examples of phase distributions and the corresponding histograms at different anisotropic factors when $d = 0.5\,mm$. (a-h) $g = 0.98, 0.96, 0.94, 0.92, 0.90, 0.80, 0.60, and\ 0.40$, respectively.

Same as for the ground glass, transverse coherence length κ and height deviation σ were used to characterize the phasemask. Table 1 shows the calculated results of κ, σ, and their ratio corresponding to Figs. 3&4. Note that for phasemasks we can only calculate its standard deviation $\Delta\Psi$ in phase, and σ was obtained by dividing $\Delta\Psi$ to the wavenumber k_n. $k_n = \frac{2n\pi}{\lambda}$, where the wavelength $\lambda = 0.532\ \mu m$, and the refractive index $n = 1.33$ in this study.

Table 1 Transverse coherence length κ, height deviation σ, and their ratio of the phasemasks at different g and thicknesses.

g	d=0.1 mm			d=0.5 mm		
	$\kappa\ (\mu m)$	$\sigma\ (\mu m)$	κ/σ	$\kappa\ (\mu m)$	$\sigma\ (\mu m)$	κ/σ
0.98	3.6	0.064	56.24	0.6	0.113	5.31
0.96	2.2	0.061	36.07	0.4	0.113	3.54
0.94	1.6	0.060	26.70	0.4	0.113	3.64
0.92	1.2	0.058	20.69	0.4	0.114	3.51
0.90	0.4	0.066	6.08	0.4	0.113	3.54
0.80	0.4	0.062	6.45	0.4	0.114	3.52
0.60	0.6	0.046	13.04	0.4	0.111	3.59
0.40	0.6	0.043	13.95	0.4	0.112	3.55

Clearly, the transverse coherence length decays fast with g, especially for thicker layers. The minimum transverse coherence length is the wavelength in medium, *i.e.*, $\lambda/n = 0.4\ \mu m$. For $g = 0.60$ and 0.40, however, the histograms in both Figs.3&4 are shaper comparing to other g values, and hence the corresponding σ are significantly smaller. A possible explanation is that more photons are backscattered with a small anisotropy factor, resulting in larger weight of ballistic photons in the transmitted light. Based on the table, we can see a clear trend of the phasemask with the anisotropy factor.

Fig.5a shows the time reversed intensities at different scanning angles in simulation and experiment. From the fitted curve, we can obtain the AME range based on Eq. (1). In Fig. 5b, the magenta pluses denote the AME ranges of 0.5 mm thick samples from simulation at different g, while black crosses and cyan circles represent the AME ranges of 1 mm and 1.5 mm thick samples, respectively. The fitted curves share the same formula

$$\theta = \frac{a}{(1-g)^m} + b, \tag{3}$$

where parameters a, b, and m are sensitive to thickness: $d = 0.5\ mm$, $\theta = \frac{8.23\times10^{-3}}{(1-g)^{0.9}} + 3.54 \times 10^{-2}$; $d = 1.0\ mm$, $\theta = \frac{8.36\times10^{-4}}{(1-g)^{1.2}} + 3.65 \times 10^{-2}$; $d = 1.5\ mm$, $\theta = \frac{3.51\times10^{-4}}{(1-g)^{1.3}} + 3.37 \times 10^{-2}$. Apparently, as thickness increases, the decaying of AME range with g becomes steeper, in response to a larger value of m. An interesting phenomenon is that the AME range does not monotonically decrease with g; it slightly rises at small g. A possible explanation is that weight of ballistic photons in transmission is larger with stronger backscattering (smaller g). For thick medium, the weight of ballistic photons drops exponentially with thickness and being much faster than diffused light does. Hence, there is no obvious rise for thicker samples. The yellow dots ($g = 0.95$) and green diamonds ($g = 0.98$) denote the measured AME ranges of 0.5 mm and 1 mm thick samples in experiment, respectively, agreeing with simulation quite well. From Eq.(1) we know that the AME range is proportional to a modification factor $\frac{\kappa}{\sqrt{2}(n-1)\sigma}$. For the 0.5 mm thick sample, the ratio of the AME ranges at $g = 0.98$ to $g = 0.96$ is 1.63 in Fig.5, while the ratio of κ/σ in Table 1 is 1.5. They are consistent, which is a convincing validation of the effect of the aforementioned modification factor.

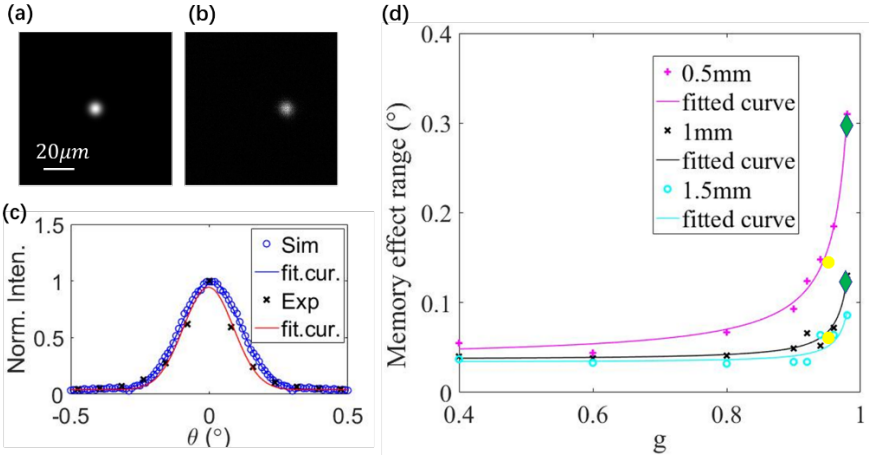

Fig. 5 Simulation and experiment results. (a,b) Images of time reversed focus at scanning angles $\theta = 0°$ and $0.1°$, respectively. (c) Intensities of time reversed focus at different angles in simulation (blue circles) and experiment (black crosses), as well as their Gaussian fitted curves (95% confidence bounds). Sample thickness was 0.5 mm. (b) Simulation and experiment results of the AME range as a function of anisotropic factor g at different thicknesses. The simulation

data of $d = 0.5mm$, 1mm, and 1.5mm are represented by magenta pluses, black crosses, and cyan dots, respectively. The green diamonds and yellow dots are measured values in experiment.

Thus far, it can be concluded that forward scattering domination and certain portions of ballistic photons are two preconditions for the AME; at least one should be satisfied to yield the AME phenomenon. It also determines when (conditions) and where (field of view) the AME can be used for optical imaging and manipulation through scattering media.

4. Discussion and conclusion

From the perspective of differentiation, once the output itself is distinguishable without any external references, the spatial shift invariance is broken, and there is no more AME. For a scattering layer simulated by two random phasemasks, the wavefront after the 1st phasemask is scrambled with fine structures; when such scrambled wavefront meets the 2nd phasemask, because of its phase distribution, a shift of the wavefront can be differentiated. For a pure plane without any structures, it does not have the ability to distinguish any change of the incident wavefront. If the 2nd phasemask has finer grains, the resolution is higher, and consequently the AME range is smaller. Since the characteristic size, *i.e.*, the transverse coherence length of the wavefront on the plane of 2nd phasemask, is proportional to the thickness according to van Cittert-Zernike Theorem [41], it will be easier to differentiate a wavefront with longer transverse coherence length. Intuitively, the resolution is inversely proportional to the thickness. The upper limit of the angular resolution of the system is its AME range.

We must point out a shortcoming of the modified multiple-random-phasemask model. Due to the constraint in generating the phasemasks, the maximum standard deviation in phase $\Delta\Psi$ is $\frac{\pi}{\sqrt{3}}$, and the maximum height deviation $\sigma = 0.1155\,\mu m$ in our case. Considering the minimum grain size is 0.4 μm and the minimum of the modifying factor $\frac{\kappa}{\sqrt{2}(n-1)\sigma} = 7.4$, the simulated AME range will be at least 7.4 folds of the calculated value according to $\theta = \frac{\lambda}{2\pi d}$. In fact, all multiple-random-phasemask models have similar inaccuracy. A tricky situation is that the AME range of a thick sample is too small to be measured accurately. Hence, it is difficult to verify and correct the modification factor. That said, usually it does not cause any operational problem since we are interested in the AME only when its range is big enough. Nevertheless, we should keep it in mind in application.

In summary, we studied the influence of anisotropy factor g on phasemask and the AME range in this study. An empirical relationship among the AME range, thickness, and g was found. As g approaches 1, the enhancement in AME range is significant. However, increasing sample thickness diminishes the dependence on g quickly. The investigation shows that it is only meaningful to make use of the AME when ballistic photons or forward scattering dominate in light propagation, *i.e.,* the penetration thickness is within one transport mean free path. Recent progress in adaptive optics, two/three-photon microscopy, structure illumination microscopy [44,45], and photoacoustic microscopy [46,47] has allowed one to see clearer and deeper into biological tissues. Field of view of these implementations, however, need to be further expanded *in vivo*. Our study, together with optimized wavefront compensation against the scattering-induced phase distortions in biological tissue, provides a reference to maximize the field of view of various microscopies, and light manipulation techniques [48] as well.

Disclosures

The authors declare no conflict of interests.

Funding

This work was supported by National Natural Science Foundation of China (61571427, 81930048, and 81671726).

References

1. S. Feng, C. Kane, P. A. Lee, and A. D. Stone, “Correlations and fluctuations of coherent wave transmission through disordered media,” Phys. Rev. Lett. 11, 834-837 (1988).
2. I. Freund, M. Rosenbluh, and S. Feng, “Memory effects in propagation of optical waves through disordered media,” Phys. Rev. Lett. 61, No.20, 2328-2331 (1988).
3. J. Bertolotti, E. G. van Putten, C. Blum, A. Lagendijk, W. L. Vos, and A. P. Mosk, "Non-invasive imaging through opaque scattering layers," Nature 491, 232-234 (2012).
4. O. Katz, P. Heidmann, M. Fink, and S. Gigan, “Non-invasive single-shot imaging through scattering layers and around corners via speckle correlations,” Nat. photon. 8, 784-790 (2014).
5. M. Cua, E. Zhou, and C. Yang, “Imaging moving targets through scattering media,” Opt. Express 25, 3935-3945 (2017)
6. W. Yang, G. Li, and G. Situ, “Imaging through scattering media with the auxiliary of a known reference object,” Scientific Reports 8, 9614(1-7) (2018).
7. C. Guo, J. Liu, T. Wu, L. Zhu, and X. Shao, “Tracking moving targets behind a scattering medium via speckle correlation,” Appl. Opt. 57(4), 905-913, (2018).
8. H., Liu, X. Wang, J. Gao, T. Yu, and S. Han, “Seeing through dynamics scattering media: Suppressing diffused reflection based on decorrelation time difference,” J Innov. Opt. Health. Sci. 2(4), 1942001(1-7), (2019).
9. C. Guo, J. Liu, W. Li, T. Wu, L. Zhu, J. Wang, G. Wang, and X. Shao, “Imaging through scattering layers exceeding memory effect range by exploiting prior information,” Opt. Comm. 434, 203-208(2019).
10. X. Wang, X. Jin, J. Li, X. Lian, X. Ji, and Q. Dai, “Prior-information-free single-shot scattering imaging beyond the memory effect,” Opt. Lett. 44, 1423-1426 (2019).
11. M. Chen, H. Liu, Z., Liu, P. Lai, and S. Han, “Expansion of the FOV in speckle autocorrelation imaging by spatial filtering,” Opt. Lett. 44, 5997-6000 (2019).
12. H. Zhuang, H. He, X. Xie, and J. Zhou, “Hight speed color imaging through scattering media with a large field of view,” Sci. Rep. 6, 32696(1-7), (2016).
13. X. Xu, H. Liu, and L. V. Wang, "Time-reversed ultrasonically encoded optical focusing into scattering media," Nat. Photon. 5(3) 154-157 (2011).
14. P. Lai, L. Wang, J. W. Tay, and L. V. Wang, "Photoacoustically guided wavefront shaping (PAWS) for enhanced optical focusing in scattering media," Nature Photonics 9, 126-132 (2015).
15. J. Ryu, M. Jang, T. J. Eom, C. Yang, and E. Chung, “Optical phase conjugation assisted scattering lens: variable focusing and 3D patterning,” Sci. Rep. 6, 23494 (2016).
16. Z. Yu, M. Xia, H. Li, T. Zhong, F. Zhao, H. Deng, Z. Li, D. Wang, and P. Lai, "Implementation of digital optical phase conjugation with embedded calibration and phase rectification", Sci. Rep. 9, 1537 (2019)
17. G. S. He, “Optical phase conjugation: principles, techniques, and applications. Progress in Quantum Electronics” 26(3), 131-191 (2002).
18. R. K. Tyson, Principles of Adaptive Optics 4th edn (CRC Press, Boca Raton, 2010).
19. E. G. van Putten, D. Akbulut, J. Bertolotti, W. L. Vos, A. Lagendijk, and A. P. Mosk, “Scattering lens resolves sub-100 nm structures with visible light,” Phys. Rev. Lett. 106, 193905 (2011).
20. I. M. Vellekoop, and A. P. Mosk, “Focusing coherent light through opaque strongly scattering media,” Opt. Lett. 32, 2309–2311 (2007).
21. X. Yang, Y. Pu, and D. Psaltis, “Imaging blood cells through scattering biological tissue using speckle scanning microscopy,” Opt. Express 22, 3405–3413 (2014).
22. S. Schott, J. Bertolotti, J. L´eger, L. Bourdieu, and S. Gigan, “Characterization of the angular memory effect of scattered light in biological tissues,” Opt. Express. 23, 13505, (2015).
23. B. Judkewitz, R. Horstmeyer, I. M. Vellekoop, I. N. Papadopoulos, and C. Yang, “Translation correlations in anisotropically scattering media,” Nat. phys. 11, 684 (2015).

24. G. Osnabrugge, R. Horstmeyer, I. N. Papadopoulos, B. Judkewitz, and I. M. Vellekoop, “Generalized optical memory effect,” Optica 4, 886 (2017).

25. H. Yilmaz, C. W. Hsu, A. Yamilov and H. Cao, “Transverse localization of transmission eigenchannels,” Nature Photonics 13, 352-358 (2019).

26. L. Zhu, J. B. de Monvel, P. Berto, S. Brassselet, S. Gigan, and M. Guillon, “Chromato-axial memory effect through a forward-scattering slab,” Optica, 7(4), 338-345 (2020).

27. H. Liu, M. Chen, Z. Liu, S. Han and L. V. Wang, “Physical picture of the optical memory effect,” Photonics Research 7, 1323-1330, (2019).

28. Z. Kam, P. Kner D. Agard, and J. W. Sedat, “Modelling the application of adaptive optics to wide-field microscope live imaging,” J. Microsc 226(Pt 1), 33-42 (2007).

29. D. Débarre, E. J. Botcherby, T. Watanabe, S. Srinivas, M. J. Booth, and T. Wilson, “Image-based adaptive optics for two-photon microscopy,” Opt. Lett 34(16), 2495-2497 (2009).

30. O. Katz, E. Small and Y. Silberberg, “Looking around cornoers and through thin turbid layers in real time with scattered incoherent light,” Nature Photon. 6, 549-553 (2012).

31. J. Park, C. Park, H. Yn, Y. Cho, and Y. Park, “Dynamic active wave plate using random nanoparticles,” Opt. Express 20(15), 17010-17016 (2012).

32. G. Ghielmetti, and C. M. Aegerter, “Scattered light fluorescence microscopy in three dimensions,” Opt. Express 20(4), 3744-3752 (2012).

33. T. R. Hillman, T. Yamauchi, W. Choi, R. R. Dasari, M. S. Feld, Y. Park, and Z. Yaqoob, "Digital optical phase conjugation for delivering two-dimensional images through turbid media," Scientific reports 3, 1909 (2013).

34. L. Kong, M. Cui, “In vivo fluorescence microscopy via iterative multi-photon adaptive compensation technique,” Opt. Express 22(20), 23786-23794 (2014).

35. J. Mertz, H. Paudel, and T.G. Bifano, “Field of view advantage of conjugate adaptive optics in microscopy applications,” Appl. Opt. 54(11), 3498-3506 (2015).

36. J.-H. Park, W. Sun, and M. Cui, “High-resolution in vivo imaging of mouse brain through the intact skull,” PNAS 112(30), 9236-9241 (2015).

37. J. Ryu, M. Jang, T. J. Eom, C. Yang, and E. Chung, "Optical phase conjugation assisted scattering lens: variable focusing and 3D patterning," Scientific reports 6, 23494 (2016).

38. W. Zheng, Y. Wu, P. Winter, R. Fisher, D. D. Nogare, A. Hong, C. McCormick, R. Christensen, W. P. Dempsey, D. B. Arnod, J. Zimmerberg, A. Chitnis, J. Sellers, C. Waterman, and H. Shroff. “Adaptive optics improves multiphoton super-resolution imaging,” Nature Methods 14(9), 869-875 (2017).

39. V. Tuchin, Tissue Optics: Light Scattering Methods and Instruments for Medical Diagnosis, 2nd edn (SPIE, Bellingham, Washington, 2007).

40. L. V. Wang, and H.-i.Wu. Biomedical Optics: Principles and Imaging (John Wiley & Sons, Inc., Hoboken, New Jersey, 2007).

41. M. Qiao, H. Liu, G. Pang, and S. Han, "Non-invasive three-dimension control of light between turbid layers using a surface quasi-point light source for precorrection," Scientific reports 7, 9792 (2017).

42. I. Yamaguchi and T. Zhang, "Phase-shifting digital holography," Optics letters 22, 1268-1270 (1997).

43. J. W. Goodman. Statistical optics, 2nd ed (John Wiley & Sons, Inc., New York, 2015).

44. F. Ströhl, and C. F. Kaminski, “Frontiers in structured illumination microscopy,” Optica 3(6), 667-677 (2016).

45. R. Heintzmann, and T. Huser, Super-resolution structured illumination microscopy. Chem. Rev.117(23), 13890-13908 (2017).

46. Yingying Zhou, Siyi Liang, Mingsheng Li, Jianbo Chen, Chengbo Liu, Puxiang Lai, and Lidai Wang, "Optical-resolution photoacoustic microscopy with ultrafast dual-wavelength excitation", Journal of Biophotonics, e201960229 (2020).

47. Yingying Zhou, Fei Cao, Huanhao Li, Xiazi Huang, Dongshan Wei, Lidai Wang, and Puxiang Lai, "Photoacoustic imaging of microenvironmental changes in facial cupping therapy", Biomedical Optics Express 11(5), 2394-2401 (2020).

48. H. Misawa, M. Koshioka, K. Sasaki, N. Kitamura, and H. Masuhara, “Three-dimensional optical trapping and laser ablation of a single polymer latex particle in water,” J. Appl. Phys. 70, 3829–3836 (1991).